SCIENTIFIC REPORTS

OPEN

Band-gap-graded $Cu_2ZnSn(S_{1-x},Se_x)_4$ Solar Cells Fabricated by an Ethanol-based, Particulate Precursor Ink Route

Kyoohee Woo[1], Youngwoo Kim[1], Wooseok Yang[1], Kyujin Kim[1], Inhyuk Kim[1], Yunjung Oh[1], Jin Young Kim[2] & Jooho Moon[1]

[1]Department of Materials Science and Engineering, Yonsei University, 50 Yonsei-ro, Seodaemun-gu, Seoul 120-749, Republic of Korea, [2]Photo-Electronic Hybrids Research Center, Korea Institute of Science and Technology (KIST), Hwarangno 14-gil 5, Seongbuk-gu, Seoul 136-791, Republic of Korea.

Correspondence and requests for materials should be addressed to J.M. (jmoon@yonsei. ac.kr)

Solution processing of earth-abundant $Cu_2ZnSn(S_{1-x},Se_x)_4$ (CZTSSe) absorber materials is an attractive research area in the economical and large-scale deployment of photovoltaics. Here, a band-gap-graded CZTSSe thin-film solar cell with 7.1% efficiency was developed using non-toxic solvent-based ink without the involvement of complex particle synthesis, highly toxic solvents, or organic additives. Despite the high series resistance due to the presence of a thick $Mo(S,Se)_x$ layer and $Zn(S,Se)$ aggregates, a high short-circuit current density (J_{SC}) was generated. In addition, there was no significant difference in open circuit voltages (V_{OC}) between CZTS (0.517 V) and CZTSSe (0.505–0.479 V) cells, despite a significant band gap change from 1.51 eV to 1.24 eV. The high J_{SC} and less loss of V_{OC} are attributed to the effect of band gap grading induced by Se grading in the CZTSSe absorber layer. Our environmentally benign ink approach will enable the realization of low-cost, large-area, high-efficiency thin-film solar cells.

T hin-film chalcogenide photovoltaic (PV) technologies could allow for the widespread adoption of solar energy because they offer exceptional opportunities for high-performance, large-area module production[1–3]. In particular, $Cu(In,Ga)(S,Se)_2$ (CIGSSe) and CdTe technologies with cell efficiencies (12 ~ 20%) have improved nearly to the point of commercialization[4–6]. However, the involvement of the heavy metal Cd and rare metals such as indium (In), germanium (Ga), and tellurium (Te) in the composition is the main obstacle to the widespread use of these technologies. In this regard, kesterite Cu_2ZnSnS_4 (CZTS) is currently one of the key functional materials in thin-film photovoltaics due to its abundance and nontoxicity, which are important criteria for the economical, large-scale deployment of photovoltaics[7–10]. In addition, the optical and electronic properties of CZTS are similar to those of CIGS and CdTe, which produce sustainable, high-performance solar cells.

Since 2010, high-efficiency (>7%) CZTS photovoltaics have been successfully demonstrated by several research groups using different approaches, including thermal co-evaporation[11], sputtering[12], electrodeposition[13], and solution processes employing nanocrystal ink[14] or hydrazine-based ink[15–17]. In the case of vacuum-based techniques, the integration of multiple evaporation or sputtering sources provides versatility, leading to good control over the film composition and corresponding phase profile. However, vacuum-based techniques require a large capital investment and a considerable amount of energy to deposit the films from the target sources. Furthermore, these techniques suffer from relatively slow throughput and low material utilization[18,19]. Therefore, solution-based deposition methods, which have several advantages such as suitability for use with large-area substrates, high throughput, and efficient material use, are being developed. Among the various methods, the highest efficiency of 11.1% was achieved in 2012 using a hydrazine-based deposition process, thereby demonstrating the potential of solution-based processing to compete with vacuum-deposition approaches in terms of cost and performance[15].

In the hydrazine precursor route, because the elemental constituents of CZTS are partially or fully dissolved in solvent without any additive, it is beneficial to fabricate high-purity and precisely stoichiometric-controlled CZTS. However, due to the presence of the highly toxic and dangerously unstable hydrazine solvent, all processes for ink and film preparation should be performed under inert atmosphere. As a result, it is difficult to adapt this

process for low-cost and large-scale solar cell fabrication. Therefore, decreasing the hydrazine concentration or precluding its use is necessary. In this regard, we recently reported a simple solution-based deposition approach using a nontoxic solvent (ethanol)-based ink composed of commercially available particulate precursors, such as copper (I) sulfide (Cu_2S), zinc (Zn), tin (Sn), and sulfur (S), and a CZTS solar cell with an efficiency of 5.1% was obtained[20]. These preliminary results indicate that our approach is potentially viable for fabricating CZTS solar cells without the use of complex particle synthesis, highly toxic solvents, or organic additives, although the efficiency of the technique must be improved. Here, we address the efficiency-limiting challenges and problems encountered in our previously reported devices[20]. Significant improvements in power conversion efficiency (PCE) are demonstrated for the first time by employing the band-gap-graded $Cu_2ZnSn(S_{1-x},Se_x)_4$ (CZTSSe) layer that arises from Se grading, and an effective area (0.21 cm², excluding the shaded areas by the evaporated Ni/Al contacts) PCE of 7.1% is achieved under air mass (AM) 1.5 illumination. We investigate the influence of band gap grading on the characteristics of CZTSSe cells. Grazing incidence X-ray diffraction (GIXRD) analysis allows us to confirm the grading of Se present in the CZTSSe absorber layer.

Results

CZTS thin films were fabricated by a nontoxic solution process, as described in our previous report[20]. Slurries containing four different components in the forms of Cu_2S, Zn, Sn, and S particles at 0.4 M were prepared using ethanol, and the formulated inks were milled for 24 h. CZTS precursor films were deposited on 1-μm molybdenum (Mo)-coated soda lime glass by spin coating. To avoid crack formation within the CZTS precursor films, multiple thin layers were applied. The as-prepared films were then annealed at 530°C under a nitrogen (N_2) + hydrogen sulfide (H_2S) (5%) atmosphere for sulfurization and were subsequently annealed at 500°C under selenium (Se) vapor for 20 min in a graphite box to form the Cu_2Zn $Sn(S_{1-x},Se_x)_4$ (CZTSSe) films. The morphologies of the CZTSSe films were investigated by scanning electron microscopy (SEM), as shown in Fig. 1a. Large, micron-sized, densely packed grains were observed. The XRD analysis confirmed the formation of a crystalline quaternary semiconductor, as presented in Fig. 1b. The sharp peaks of the sulfurized CZTS film (red) at 2θ = 28.45°, 47.3°, and 56.2° are in good agreement with the diffraction of the (112), (220), and (312) planes of CZTS (JCPDS no. 26-0575), respectively, which clearly indicates the perfect kesterite structure of CZTS. In the case of the selenized CZTSSe film (blue), the 2θ values of the major peaks of the (112), (220), and (312) planes were shifted toward lower angles due to the larger unit cell lattice parameters of the CZTSSe with S sufficiently replaced by Se. Furthermore, as shown in the enlargement of the 2θ-angle range from 26° to 29°, broad peaks at 2θ = 27.8° and 28.3° with low intensities were detected (as indicated by arrows), reflecting the presence of secondary phases. These phases would be less Se-replaced CZTSSe and/or close to phase-pure CZTS. They are either distributed over the Se-rich CZTSSe film or segregated, as X-ray diffraction measurement using the conventional θ/2θ scanning method only provides spatially-averaged phase information. We assume the presence of segregation with a grading of Se from top to bottom across the CZTSSe absorber layer. This Se grading presumably arises from inconstant Se partial pressure conditions during the selenization process. At the initial stage of selenization, a high Se vapor pressure can develop as the Se source in a graphite box is vaporized when loaded into a preheated tube furnace. This pressure will drop as selenization proceeds because Se vapor escapes from the unsealed graphite box. Annealing under this non-uniform Se vapor condition likely results in Se grading inside the CZTSSe layer (Supplementary Fig. S1). The depth distributions of Cu, Zn, Sn, S, Se and Mo were also analyzed by a secondary ion mass spectroscopy (SIMS) (Supplementary Fig. S2), which confirms the Se grading from the surface to bottom.

The Se-graded CZTSSe absorber layer (~0.78 μm) described herein is employed for fabrication of a complete thin-film solar cell with a standard structure. Cadmium sulfide (CdS) (~60 nm) was deposited using a chemical bath method, and intrinsic zinc oxide (i-ZnO) (~50 nm) and indium tin oxide (ITO) (~200 nm) were then sputtered, as shown in Fig. 2a. In addition, the CZTSSe films possessed a bimodal grain distribution, where large grains are located at the top of the absorber layer, and somewhat smaller grains are located near the bottom. The current-voltage (J-V) characteristics for selected CZTSSe solar cells (CZTSSe #1–#5) measured under AM 1.5 illumination are presented in Fig. 2b and Table 1. The best CZTSSe thin-film solar cell exhibited an effective area efficiency of 7.17% [open-circuit voltage (V_{OC}) = 0.505 V, short-circuit current density (J_{SC}) = 24.55 mA cm⁻², fill factor (FF) = 57.8%], representing high efficiency comparable with those reported for air-stable and nontoxic solution-based CZTSSe thin-film solar cells[14,21,22]. The J-V curves of other devices gave power conversion efficiencies of 6–7%.

Compared with the performance of the CZTS solar cell [efficiency = 5.14%, V_{OC} = 0.517 V, J_{SC} = 18.86 mA cm⁻², FF = 52.8%]
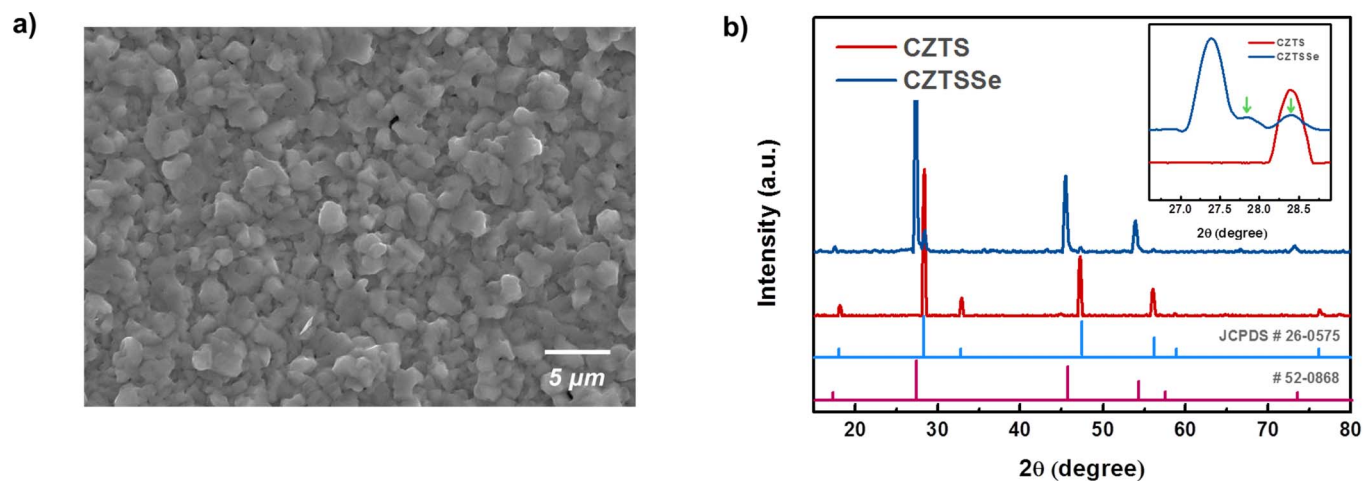

Figure 1 | Microstructure and phase analysis for selenized CZTSSe films. (a) Scanning electron microscope (SEM) images of selenized CZTSSe films in an in-plane view. The precursor CZTS films are annealed at 530°C under a N_2 + H_2S (5%) atmosphere in a tubular furnace and are then annealed under Se vapor at 500°C for 20 min in a graphite box to form the CZTSSe absorbing layer. (b) XRD analysis of the sulfurized CZTS film (red) and selenized CZTSSe films (blue). The enlargement of the 2θ-angle range from 26° to 29° shows the (112) peak positions of CZTS and CZTSSe films.
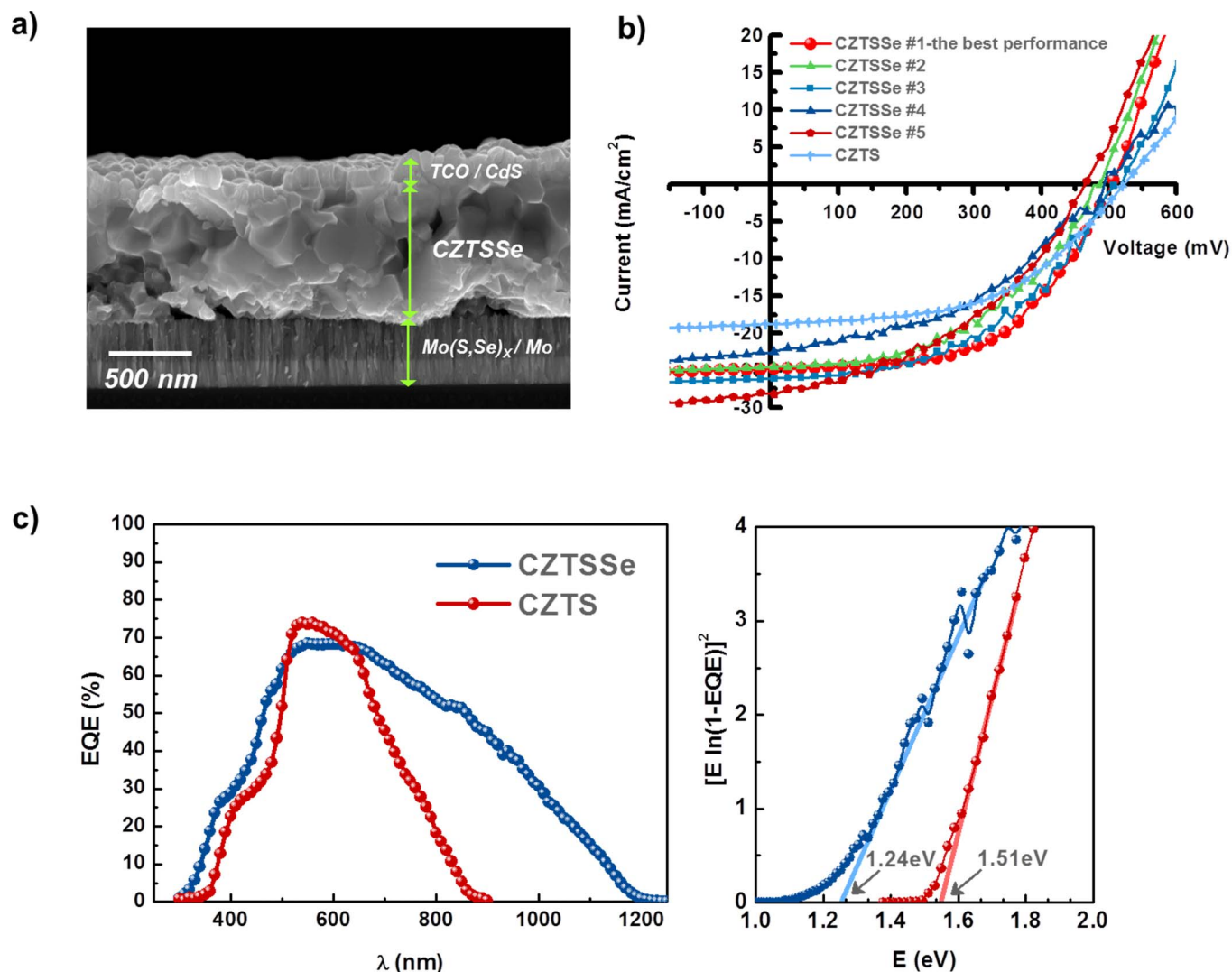
Figure 2 | Characterization of CZTSSe thin-film solar cells. (a) Cross-sectional image of the Se-graded CZTSSe thin-film solar cell. (b) J-V characteristics for the Se-graded CZTSSe thin-film solar cells compared to the previously reported CZTS device[20]. All CZTSSe samples (#1 ∼ #5) were fabricated under the same process conditions, but produced in different batches. All device performance parameters are based on the effective area (0.21 cm²), excluding the area shaded by the Ni/Al finger electrode. (c) The EQE curve of the Se-graded CZTSSe thin-film solar cells compared with the CZTS device. The band gap of the CZTSSe and CZTS absorber layer is determined to be 1.24 eV and 1.51 eV, respectively, from a plot of $[E \ln (1 - EQE)]^2$ versus E.

described in our previous work[20], the short-circuit current density of the CZTSSe cell increased considerably. Fig. 2c shows the external quantum efficiency (EQE) of the CZTSSe solar cell as a function of photon wavelength. For comparison purposes, we also include the data for our previous CZTS cell[20]. The EQE spectrum at short wavelengths (below ∼ 500 nm) indicates similar absorption originating from the CdS/i-ZnO/ITO top layers between CZTS and CZTSSe cells. The CZTSSe cell has a longer cut-off wavelength, extending

to approximately 1,200 nm, whereas the photon response of the CZTS cell stops at approximately 900 nm. Typically, the band gap of pure S-based CZTS varies from 1.48–1.6 eV, in contrast with Se-based CZTSe, the band gap of which is lower, in the range of 1.0–1.2 eV. The band gaps determined from the EQEs of the CZTSSe and CZTS devices are approximately 1.24 eV and 1.51 eV, respectively, which are in reasonable agreement with reported values[24]. In other words, the replacement of S with Se in the absorber lowered the band

Table 1 | Device characteristics of the particulate precursor derived CZTSSe cells by non-toxic solution process

Cell	PCE [%]	FF [%]	V_{OC} [mV]	J_{SC} [mA cm^{-2}]	R_s[a] [Ωcm²]	R_{sh}[b] [Ωcm²]	E_g/q-V_{OC} [mV]
CZTSSe #1	7.17	57.83	505.4	24.5	13.20	1525.1	240
CZTSSe #2	6.58	50.23	499.9	26.2	14.57	1088.6	-
CZTSSe #3	6.28	50.09	507.4	24.7	15.30	1154.9	-
CZTSSe #4	5.98	48.75	489.1	24.6	23.83	1079.5	-
CZTSSe #5	5.83	46.56	479.6	26.1	26.42	967.7	-

[a]Series resistance (R_s) determined by Sites' method using J-V data under illumination[23].
[b]Shunt resistance (R_{sh}) is the change in the voltage for change in the current density ($\Delta V_{reverse\ bias}/\Delta J_{reverse\ bias}$) at 0 V in dark J_{SC}-V_{OC} curve.

gap from 1.51 eV (CZTS) to 1.24 eV (CZTSSe), which had a remarkable impact on the increase in the photogenerated current, resulting in a significantly improved efficiency compared with CZTS (PCE = 5.14%). It should also be noted that, in comparison with the smooth curve of the CZTS cell, a plot of $[E \ln (1 - EQE)]^2$ versus E for the CZTSSe cell shows a discontinuous rugged curve in which many linear regions can be observed. This rugged curve shape indicates that CZTSSe film can have multiple band gaps due to small variations in the S/Se ratio of the film.

The temperature dependence of J-V under AM 1.5 illumination for the CZTSSe device is investigated to understand potential loss mechanisms that limit the device performance, as shown in Fig. 3a. Lowering the temperature steadily increased the open circuit voltage, but the fill factor and short circuit current dropped dramatically, causing an efficiency collapse. The temperature dependencies of V_{OC} and J_{SC} are presented in Fig. 3b. The relationship between V_{OC} and temperature (T) is given as[25]:

$$V_{OC} = \frac{E_A}{q} - \frac{AkT}{q} \ln \frac{J_{OO}}{J_L}$$

where E_A, A, J_{OO}, and J_L are the activation energy of the dominant recombination mechanism, diode ideality factor, reverse saturation current prefactor, and photocurrent, respectively. The activation energy for the main recombination process, $E_A = qV$ ($\sim$1.0 eV), can be extracted from the extrapolation of V_{OC} to 0 K, which is lower than the band gap value (1.24 eV) obtained from the EQE data. This discrepancy implies that the recombination mechanism in the CZTSSe cell is dominated by interface recombination causing a V_{OC} deficit, as observed in other reports[13,26]. The dominant interface recombination could occur when "cliff-like" band alignment occurs at the CdS/CZTSSe interface. Furthermore, the efficiencies of our cells are predominantly limited by the low fill factor and diminished short-circuit current at low temperatures, as observed in Table 1 and Fig. 3b. These conditions are associated with a high series resistance (R_s) of over 10 $\Omega \cdot$cm^2, which is 3–10 times larger than the values of other high-efficiency solar cells[16]. This high R_s in our cell can be ascribed to the presence of a contact barrier at the interface between the Mo and the CZTSSe. The contact barrier likely arises from the formation of a thick Mo(S,Se)$_x$ layer during sulfurization or selenization between the Mo and the CZTSSe layer.

To investigate the phase uniformity of the Se-graded CZTSSe absorber, a CZTSSe cell cross-sectioned by a focused ion beam (FIB) was investigated by high-resolution transmission electron microscopy (HR-TEM) (Supplementary Fig. S3). We observed occasional large voids (the brightest region) within the CZTSSe absorber layer and a thick Mo(S,Se)$_x$ layer ($\sim$220 nm) at the interface between Mo and the CZTSSe thin film, accounting for the observed high series resistance. In addition to such distinct microstructural features, the brightness contrast in the TEM cross-sectional image is nonuniform, possibly indicative of the presence of secondary phases between the CdS/transparent conducting oxide (TCO) and Mo(Se,Se)$_x$. It is believed that nonuniformity in contrast arises from uneven TEM specimen thickness. The presence of pores in the absorber layer makes it difficult to achieve a uniform thickness using FIB-assisted sample preparation. We observed the same selective area electron diffraction (SAED) patterns corresponding to kesterite CSZTSSe regardless of the locations of the regions of different brightness contrast (Supplementary Fig. S4). To gain a detailed understanding of the phase distribution of the CZTSSe film, we performed a composition mapping analysis at both the front and back interfaces, as shown in Fig. 4. At the front interface, the composition distribution of the Cu, Zn and Sn constituent components is uniform across depth, showing no difference in color brightness, even in the region where contrast is present in the TEM image. In addition, the brightness of Se gradually decreases from the surface to the inner regions. This observation implies the formation of uniform CZTSSe in the upper absorber layer, and grading of Se is present, which is in good agreement with the SAED analysis (Supplementary Fig. S4) and the SIMS result (Supplementary Fig. S2). However, at the back interface of the CZTSSe absorber layer with small grains, a bright domain in the composition map of Zn was detected, indicating a lump of Zn. Although the Zn(S,Se) secondary phase is clearly indistinguishable by XRD analysis (Fig. 1b) due to the overlap of the Bragg peaks with those of the CZTSSe, the slight differences in the brightness of Cu and Sn at the corresponding location suggests only sparse Zn-based secondary phase, i.e., Zn(S, Se) segregation at the back contact side. It is generally recognized that the Zn(S, Se) secondary phase in the bottom portion of the small-grained CZTSSe absorber layer, which has a wide band gap, plays an insignificant role in device performance, but this phase could be responsible for the high series resistance[11,27].

Discussion

Lowering the band gap by the addition of Se to CZTS helps to increase the photogenerated current, but it can also lower the open circuit voltage considerably. It has been reported in the literature that the V_{OC} of a CZTSSe cell with low S content was reduced by more than 0.1 V as compared with a CZTSSe cell with high S content or a
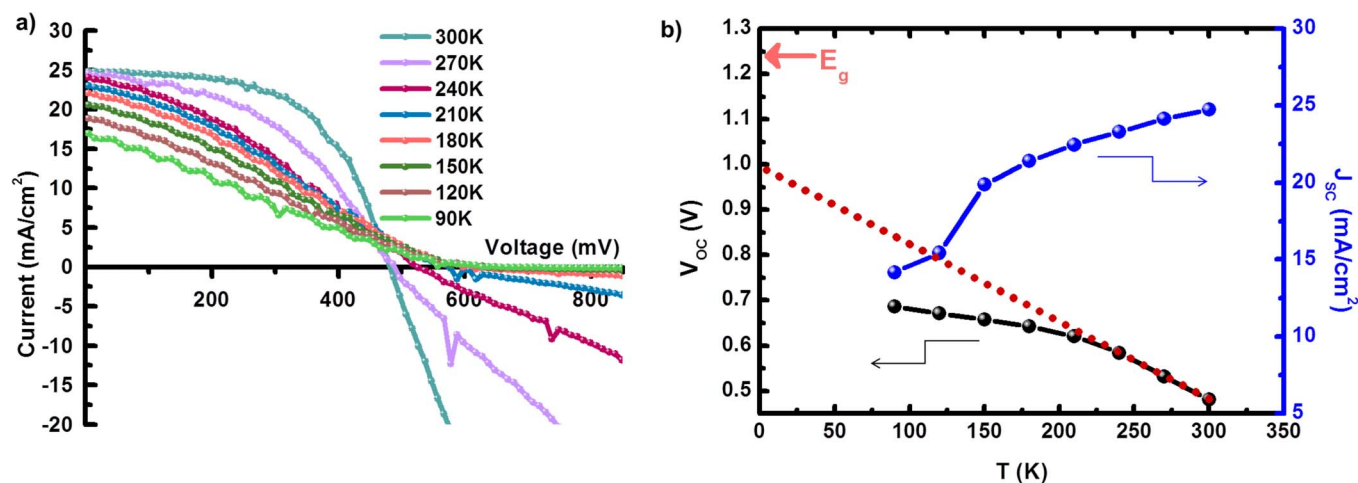

Figure 3 | Temperature-dependent (90–300 K) J-V measurement of a CZTSSe cell. (a) Temperature-dependent (90–300 K) J-V curves of a CZTSSe cell #1 under illumination (b) The corresponding temperature dependence of V_{OC} (left axis) and J_{SC} (right axis), showing extrapolation of the linear region to determine the activation energy for recombination.
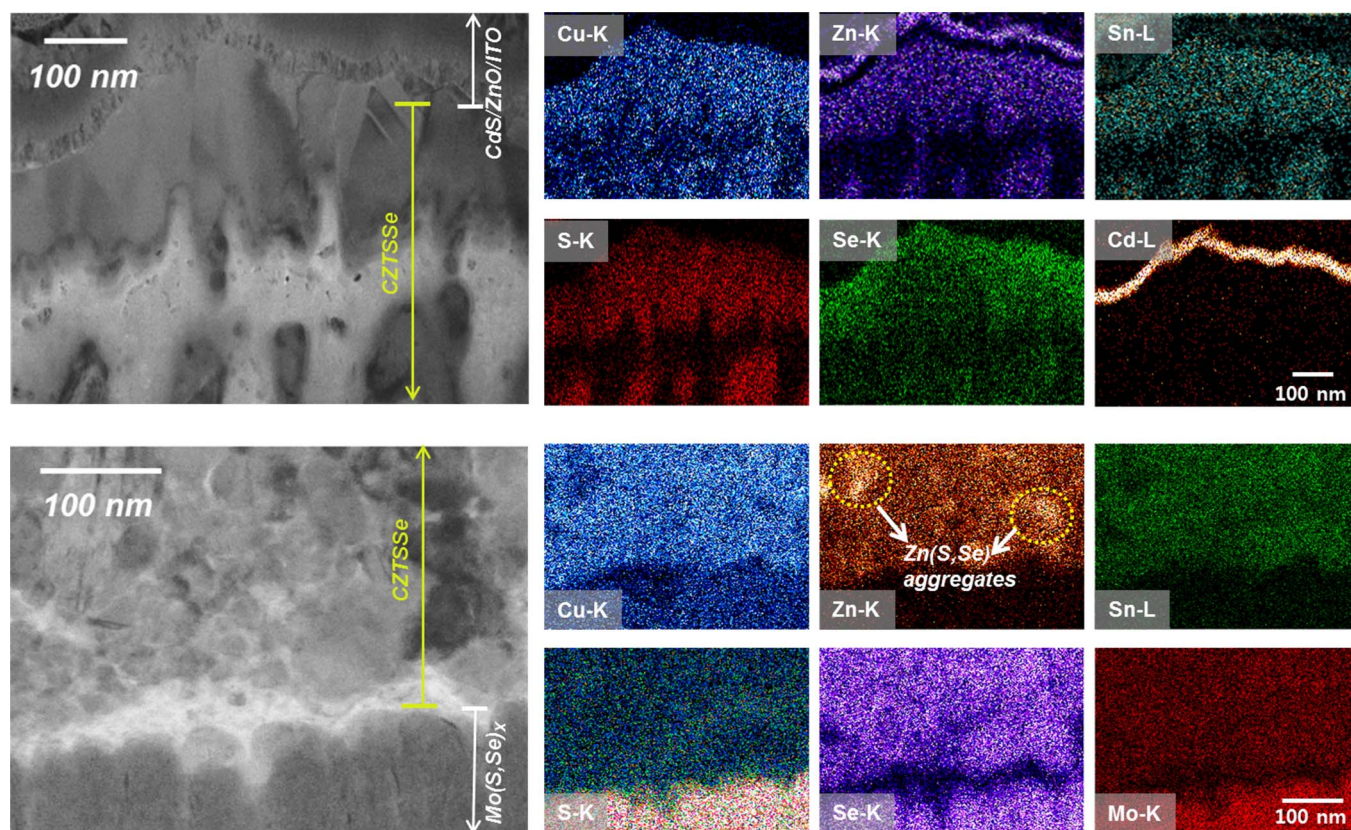
Figure 4 | TEM and composition mapping images of a cross-sectioned CZTSSe solar device consisting of Mo/Mo(S,Se)$_X$/CZTSSe/CdS/TCO (i-ZnO/ITO). The elemental map (in the same scale) revealed aggregates in the CZTSSe layer near the back contact at the interface between the CZTSSe and CdS/TCO layer (the upper image) and near the back contact (the bottom image). Zn(S,Se) aggregates are indicated by dotted circles.

pure CZTS cell[10,16]. This trend stems from strong recombination loss as the band gap decreases. However, as shown in Fig. 2b, we observed no significant difference between the open circuit voltages of CZTS (0.517 V) and CZTSSe (0.479 ∼ 0.505 V) cells despite a significant band gap change from 1.51 eV to 1.24 eV. In addition, despite the high series resistance (> 10 Ω·cm²) originating from the thick Mo(S,Se)$_x$ layer, our cell exhibited a reasonably high short-circuit current density of approximately 25 mA cm^{-2}. It is believed that these distinct features of our cell performance could be explained by the effect of band gap grading, induced by the graded Se profile in the CZTSSe absorber layer.

To understand the effect of band gap grading on the cell performance, it is necessary to examine the Se grading in our CZTSSe film. We performed GIXRD analysis with incident angles in the range from 0.2° to 20.0°. The GIXRD spectra for the (112) peak in the 2θ-angle range from 26.5° to 29.5° are shown in Fig. 5a. X-rays can penetrate deeper with increasing incident angle, thus allowing for the determination of the corresponding structural information from the surface to the inside of the films. As the incident angle increases from 0.2° to 20.0°, the (112) peak at 27.39° is shifted to a higher 2θ-angle (28.22°) and becomes broader, indicating that the Se-rich CZTSSe phase is dominant at the surface of the absorber layer and that Se content decreases in the vertical direction. The replacement reaction of S with Se occurs readily at the surface of preformed CZTS, leading to the formation of Se-rich CZTSSe phases, whereas the CZTSSe phase, which has less Se content, is present at the bottom, as the Se vapor pressure is lower.

The penetration depth of an X-ray beam into a film depends on the incident grazing angle, allowing for the estimation of depth-dependent compositional changes in the CZTSSe phase[28,29]. For the determination of X-ray penetration depth, it is necessary to calculate the

critical angle (α_c) as follows: $\alpha_c = 1 \times 10^{-3} \rho \lambda$ where ρ is the density in g cm^{-3} and λ is the wavelength in Å. For an incidence angle $\alpha < \alpha_c$, the penetration depth l is obtained from equation (1):

$$l = \frac{\lambda}{2\pi(\alpha_c^2 - \alpha^2)^{1/2}} \tag{1}$$

whereas for $\alpha > \alpha_c$, l is given by equation (2):

$$l = \frac{2\alpha}{\mu} \tag{2}$$

where μ is the absorption coefficient (CZTS ∼ 10^4 cm^{-1}). For l = 1.5418 Å (Cu Kα) and ρ = 4.56 g cm^{-3}, the critical angle α_c was calculated to be 0.6445°. The calculated penetration depths at the various incident angles are shown in Supplementary Fig. S5. At a low incident angle of 0.2°, the penetration depth is about 22 Å, and as the grazing angle is increased to 20.0°, an X-ray beam can reach a depth of about 700 nm. Because the peak arising from the Mo substrate is distinct at a grazing angle of 20.0° (Supplementary Fig. S6), the thickness of the CZTSSe absorber layer can be approximated as being 700 nm, which interestingly is close to the actual film thickness (∼780 nm) measured from the cross-sectional SEM image (Fig. 2a). Salome et $al.$ reported that the shift in the CZTSSe (112) peak follows a linear trend between those of CZTSe and CZTS, and that the peak position (x) of CZTSSe could be used to estimate the [S]/([S] + [Se]) ratio of a CZTSSe layer, which is given by the following equation[30]:

$$[S]/([Se] + [S]) = (x - 27.16)/A$$

where A is a linear factor taking the value of 1.28, which is the difference between the CZTS and CZTSe (112) peak positions of
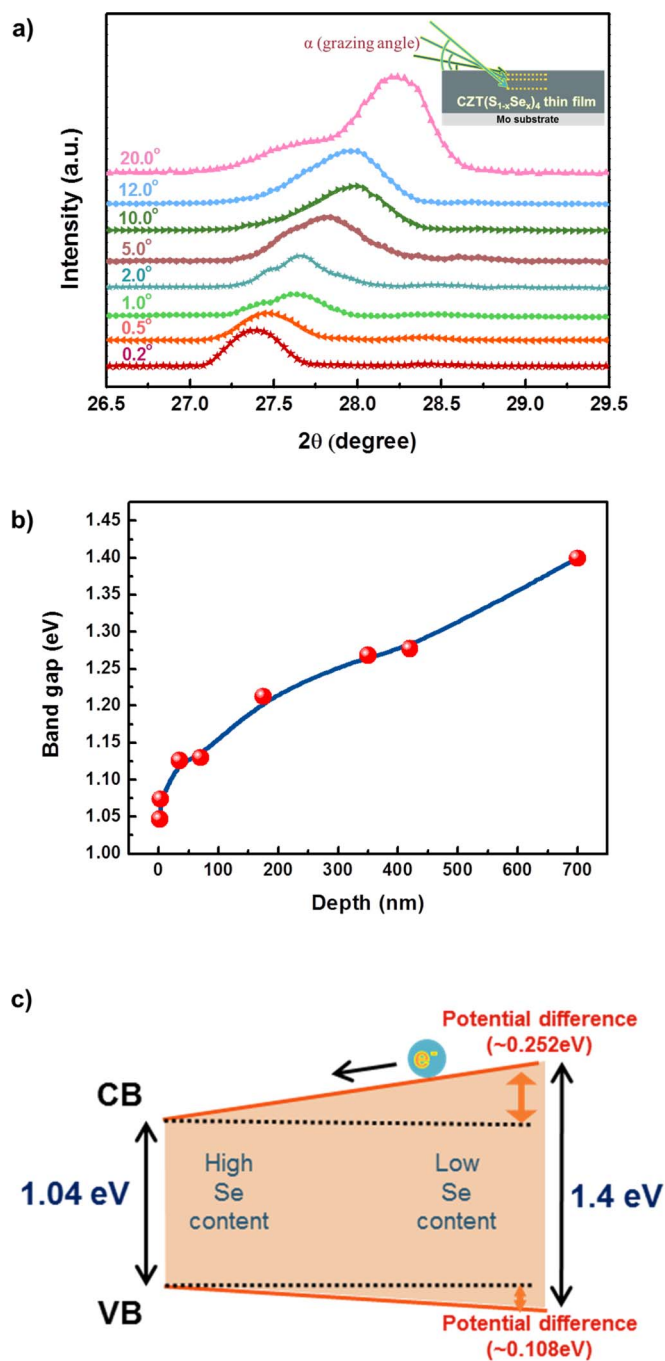
Figure 5 | Band gap grading in the Se-graded CZTSSe absorber layer.
(a) GIXRD spectra obtained with incident angles in the range from $0.2°$ to $20.0°$. The (112) peaks for CZTSSe film in the 2θ-angle range from $26.5°$ to $29.5°$ are shown. (b) The band gap variation of $Cu_2ZnSn(S_{1-x},Se_x)_4$ calculated from different S/Se ratios across the depth of the film. (c) Schematic diagram of the band alignment in the Se-graded CZTSSe absorber layer.

$28.44°$ and $27.16°$, respectively. Based on this equation, the S/Se ratio variation can be plotted as a function of penetration depth, as presented in Supplementary Fig. S7, which shows the presence of CZTSSe phases, with the value of S/Se ranging from 0.22 (at the surface) to 4.95 (near the back electrode). It is recognized that the CZTSSe band gap decreases monotonically when the Se content increases, from 1.5 eV at $x = 0$ to 0.96 eV at $x = 1$ in $Cu_2ZnSn(S_{1-x},Se_x)_4$, as estimated based on hybrid density functional theory[31,32]. The variation in the band gap of the absorber layer as a

function of film depth is plotted in Fig. 5b. The band gap of the CZTSSe phase with high Se content near the surface layer at a depth of $2 \sim 3$ nm is determined to be 1.04 eV. From the surface to the bottom, there is a decrease in the Se content of the CZTSSe phase, and the band gap subsequently increases to ~ 1.4 eV, close to the value of CZTS. As depicted in Supplementary Fig. S8, $Cu_2ZnSnSe_4$ has a higher valence band (VB) and a lower conduction band (CB) compared with Cu_2ZnSnS_4[24,25]. The conduction band offset is relatively larger (~0.35 eV) than the valence band offset (~0.15 eV). Therefore, as the Se content in our CZTSSe film increases, the CB downshift plays a more important role than the VB upshift. On the basis of the band gap variation with depth, we suggest the absorber layer band alignment shown in the schematic diagram in Fig. 5c. For the absorber with Se grading, the potential difference in CB between the surface and the bottom is calculated as being ~ 0.252 eV, whereas the potential difference in VB is ~ 0.108 eV. As a result, the Se content variation across the CZTSSe absorber layer might induce band gap grading, known as normal profiling[33]. For an ungraded solar cell structure, there is no drift force outside the depletion region to help the carriers move toward the junction for collection. In contrast, in a graded structure, the additional quasi-electric field present due to the potential difference in the conduction band forces the electrons in CB (in a p-type absorber) to drift toward the space-charge depletion region. Therefore, the carrier collection and the probability of minority carriers increase, contributing to enhancement of current generation. In addition, although widening the band gap of the absorber layer near the back contact can cause a loss of short-circuit current density (J_{SC}), it not only reduces the recombination rate, but also raises the open circuit voltage (V_{OC}) of the cell due to the lower recombination current at a higher band gap location. In this regard, it is considered that this enhanced carrier collection and slow recombination rate by normal band grading is responsible for less loss of open circuit voltage and high carrier collection in our CZTSSe cell.

In summary, CZTSSe thin-film solar cells with efficiencies ranging from 5.8% to 7.1% were fabricated using a nontoxic ethanol-based ink without the involvement of complex particle synthesis, highly toxic solvents, or organic additives. We investigated for the first time the influence of Se grading, which is induced by annealing under non-uniform Se vapor conditions, on CZTSSe absorber-based thin-film solar cells. A reasonably high short-circuit current density of approximately 25 mA cm^{-2} was generated despite high series resistance originating from a thick $Mo(S,Se)_x$ layer and $Zn(S,Se)$ aggregates at the interface between Mo and CZTSSe. In addition, there was no significant difference in open circuit voltage (V_{OC}) between the CZTS (0.517 V) and CZTSSe (0.505–0.479 V) cells in spite of significant band gap change from 1.51 eV to 1.24 eV. The high J_{SC} and lower loss of V_{OC} can presumably be attributed to the effect of band gap grading resulting from the gradual distribution of Se. GIXRD and composition mapping analysis confirmed the grading of Se from the surface (high Se content) to the bottom (low Se content) in the CZTSSe absorber layer, from which the local band gap profile was estimated across the film depth. This allows us to calculate the potential difference in the conduction band across the absorber layer as being ~ 0.252 eV and the potential difference in the valence band as being ~ 0.108 eV. These potential differences across the absorber layer cause normal band gap grading in the CZTSSe absorber layer, leading to enhanced carrier collection and a decrease in the recombination rate. Detrimental secondary phases and occasional pores should be avoided by fine control of the S or Se partial pressure during annealing, and thorough homogeneous mixing of the particulate precursors in the as-prepared films is necessary. In addition, a more detailed study of the band gap grading and the adoption of an improved graded band profile such as double grading will improve the performance of earth-abundant CZTSSe thin-film solar cells. Further improvements to our environmentally benign ink approach

will enable us to realize low-cost, large-area, high-efficiency thin-film solar cells.

Methods

CZTSSe film preparation and device fabrication. CZTS thin films were fabricated by a nontoxic solution process, as detailed in a previous report[20]. Slurries containing four different components in the forms of Cu_2S, Zn, Sn, and S particles (Sigma-Aldrich Co., St. Louis, MO, USA) at 0.4 M were prepared using ethanol, and the formulated inks were milled for 24 h. The CZTS precursor films were spin-coated on Mo (1 μm)-coated soda lime glass and then dried at 80°C. Four consecutive spin coatings were used to build up the films to approximately $0.8 \sim 0.9$ μm in thickness. A tubular furnace was used to anneal the CZTS films under a $N_2 + H_2S$ (5%) atmosphere at 530°C for 30 min. The flow rate of the gas was controlled at 50 cm³ min⁻¹. The prepared CZTS films were annealed at 500°C under Se vapor for 20 min in a graphite box by inserting the box (containing the CZTS film and elemental Se powders) into a preheated argon (Ar) flowing tube furnace.

For the CdS buffer layer deposition, thiourea $(SC(NH_2)_2)$ and deionized water were poured into a reactor. The ammonium hydroxide (NH_4OH) and $CdSO_4$ solution were added into a bath, and the prepared CZTSSe films on Mo-coated soda lime glass were then quickly transferred into the bath. The solution in the bath was continuously stirred at 200 rpm with a magnetic stir bar. The samples were removed from the bath, rinsed with deionized water, and dried under an N_2 stream. An i-ZnO and ITO transparent conductor layer was sputtered on top of the CdS under the following conditions: ~ 50 nm of i-ZnO (60 W RF, 1 mTorr, Ar flow), followed by ~ 200 nm of ITO (100 W RF, 1 mTorr, Ar flow). The sheet resistance of the ITO layer was measured as approximately 50 Ω/sq by a four-point probe (RS8, Bega Technologies, Daejeon, Korea).

Characterizations. The microstructures of the films were analyzed by FE-SEM (JSM-6010 LV, JEOL, Ltd., Tokyo, Japan). XRD was performed using a Bruker D8 DISCOVER model (Bruker Corporation, Billerica, MA, USA). Grazing incidence X-ray diffraction (GIXRD) analysis with incident angles in the range from 0.2° to 20.0° was performed by Ultima IV multipurpose diffraction system (Rigaku Corporation, Japan). The cell performance and EQE were analyzed by a solar simulator (Oriel Sol3A Class AAA, Newport Corporation, Irvine, CA, USA) and an incident photon conversion efficiency (IPCE) measurement device (QEX 10, PV Measurements, Inc., Boulder, CO, USA), respectively. A liquid-nitrogen-cooled temperature stage (Linkam Scientific Instruments, Tadworth, UK) was used for J-V measurements in the temperature range from 90 to 300 K. Samples for HR-TEM/EDX analysis were prepared using a FEI Helios 400S DB-FIB (FEI Company, Hillsboro, OR, USA), and HR-TEM images were captured using a Hitachi HD-2300A (Hitachi, Ltd., Tokyo, Japan).

1. Todorov, T. K., Gunawan, O., Gokmen, T. & Mitzi, D. B. Solution-processed $Cu(In,Ga)(S,Se)_2$ absorber yielding a 15.2% efficient solar cell. *Prog. Photovolt: Res. Appl.* **21**, 82–87 (2013).
2. Chirila, A. *et al.* Highly efficient $Cu(In,Ga)Se_2$ solar cells grown on flexible polymer films. *Nat. Mater.* **10**, 857–861 (2011).
3. Todorov, T. K. & Mitzi, D. B. Direct Liquid Coating of Chalcopyrite Light-Absorbing Layers for Photovoltaic Devices. *Eur. J. Inorg. Chem.* **1**, 17–28 (2010).
4. Guo, Q., Ford, G. M., Agrawal, R. & Hillhouse, H. W. Ink formulation and low-temperature incorporation of sodium to yield 12% efficient $Cu(In,Ga)(S,Se)_2$ solar cells from sulfide nanocrystal inks. *Prog. Photovolt: Res. Appl.* **21**, 64–71 (2013).
5. Jackson, P. *et al.* New world record efficiency for $Cu(In,Ga)Se_2$ thin-film solar cells beyond 20%. *Prog. Photovolt: Res. Appl.* **19**, 894–897 (2011).
6. Repins, I. *et al.* 19·9%-efficient $ZnO/CdS/CuInGaSe_2$ solar cell with 81·2% fill factor. *Prog. Photovolt: Res. Appl.* **16**, 235–239 (2008).
7. Li, J. B., Chawla, V. & Clemens, B. M. Investigating the role of grain boundaries in CZTS and CZTSSe thin film solar cells with scanning probe microscopy. *Adv. Mater.* **24**, 720–723 (2012).
8. Redinger, A., Berg, D. M., Dale, P. J. & Siebentritt, S. The consequences of kesterite equilibria for efficient solar cells. *J. Am. Chem. Soc.* **133**, 3320–3323 (2012).
9. Scragg, J. J. *et al.* A detrimental reaction at the molybdenum back contact in $Cu_2ZnSn(S,Se)_4$ thin-film solar cells. *J. Am. Chem. Soc.* **134**, 19330–19333 (2012).
10. Duan, H. S. *et al.* The role of sulfur in solution-processed $Cu_2ZnSn(S,Se)_4$ and its effect on defect properties. *Adv. Funct. Mater.* **23**, 1466–1471 (2013).
11. Shin, B. *et al.* Thin film solar cell with 8.4% power conversion efficiency using an earth-abundant Cu_2ZnSnS_4 absorber. *Prog. Photovolt: Res. Appl.* **21**, 72–76 (2013).
12. Scragg, J. J. *et al.* Rapid annealing of reactively sputtered precursors for Cu_2ZnSnS_4 solar cells. *Prog. Photovolt: Res. Appl.* doi: 10.1002/pip.2265.
13. Ahmed, S. *et al.* A High Efficiency Electrodeposited Cu_2ZnSnS_4 Solar Cell. *Adv. Funct. Mater.* **2**, 253–259 (2012).
14. Cao, Y. *et al.* High-efficiency solution-processed $Cu_2ZnSn(S,Se)_4$ thin-film solar cells prepared from binary and ternary nanoparticles. *J. Am. Chem. Soc.* **134**, 15644–15647 (2012).
15. Todorov, T. K. *et al.* Beyond 11% Efficiency: Characteristics of State-of-the-Art $Cu_2ZnSn(S,Se)_4$ Solar Cells. *Adv. Funct. Mater.* **3**, 34–38 (2013).
16. Mitzi, D. B. *et al.* The path towards a high-performance solution-processed kesterite solar cell. *Sol. Energy Mater. Sol. Cells* **95**, 1421–1436 (2011).
17. Yang, W. *et al.* Novel solution processing of high-efficiency Earth-abundant $Cu_2ZnSn(S,Se)_4$ solar cells. *Adv. Mater.* **24**, 6323–6329 (2012).
18. Habas, S. E., Platt, H. A. S., Hest, M. F. A. M. & Ginley, D. S. Low-cost inorganic solar cells: from ink to printed device. *Chem. Rev.* **110**, 6571–6594 (2010).
19. Guo, Q. *et al.* Fabrication of 7.2% efficient CZTSSe solar cells using CZTS nanocrystals. *J. Am. Chem. Soc.* **132**, 17384–17386 (2010).
20. Woo, K., Kim, Y. & Moon, J. A non-toxic, solution-processed, earth abundant absorbing layer for thin-film solar cells. *Energy Environ. Sci.* **5**, 5340–5345 (2012).
21. Ki, W. & Hillhouse, H. W. Earth-abundant element photovoltaics directly from soluble precursors with high yield using a non-toxic solvent. *Adv. Energy Mater.* **1**, 732–735 (2011).
22. Zong, K. *et al.* In-situ formed ternary-based hybrid ink for the fabrication of $Cu_2ZnSn(S,Se)_4$ solar cell absorbers. *J. Mater. Chem. A. DOI: 10.1039/ C3TA13157B* (2013).
23. Sites, J. R. & Mauk, P. H. Diode quality factor determination for thin-film solar cells. *Sol. Cells* **27**, 411–417 (1989).
24. Ahn, S. *et al.* Determination of band gap energy (E_g) of $Cu2ZnSnSe4$ thin films: On the discrepancies of reported band gap values. *Appl. Phys. Lett.* **97**, 021905 (2010).
25. Nadenau, V., Rau, U., Jasenek, A. & Schock, H. W. Electronic properties of $CuGaSe2$-based heterojunction solar cells. Part II. Defect spectroscopy. *J. Appl. Phys.* **87**, 594–602 (2000).
26. Wang, K. *et al.* Thermally evaporated $Cu2ZnSnS4$ solar cells. *Appl. Phys. Lett.* **97**, 143508 (2010).
27. Siebentritt, S. & Schorr, S. Kesterites—a challenging material for solar cells. *Prog. Photovolt: Res. Appl.* **20**, 512–519 (2012).
28. Singh, M., Low, I. M. & Asmi, D. Depth profiling of a functionally graded alumina/ calcium-hexaluminate composite using grazing incidence synchrotron-radiation diffraction. *J. Eur. Ceram. Soc.* **22**, 2877–2882 (2002).
29. Lim, G. *et al.* Grazing incidence synchrotron x-ray diffraction method for analyzing thin films. *J. Mater. Res.* **2**, 471–477 (1987).
30. Salome, P. M. P. *et al.* Growth and characterization of $Cu_2ZnSn(S,Se)_4$ thin films for solar cells. *Energy Environ. Sci.* **101**, 147–153 (2012).
31. Chen, S. *et al.* Compositional dependence of structural and electronic properties of $Cu_2ZnSn(S,Se)_4$ alloys for thin film solar cells. *Phys. Rev. B* **83**, 125201 (2011).
32. Walsh, A., Chen, S., Wei, S.-H. & Gong, X.-G. Kesterite Thin-Film Solar Cells: Advances in Materials Modelling of Cu_2ZnSnS_4. *Adv. Funct. Mater.* **2**, 400–409 (2012).
33. Gabor, A. M. *et al.* Band-gap engineering in $Cu(In,Ga)Se_2$ thin films grown from $(In,Ga)_2Se_3$ precursors. *Sol. Energy Mater. Sol. Cells* **41**, 247–260 (1996).

Acknowledgments

Author contributions

K.W. and J.M. designed this work and supervised whole experimental processes. K.W., Y.K., K.K. and I.K. carried out all experiments and measurements. K.W., W.Y. and J.M. wrote and edited the manuscript. W.Y., Y.O. and J.Y.K. discussed the results and commented on the manuscript.

Additional information